Fiducial Reference Measurements for Ground-Based DOAS Air-Quality Observations

ESA Contract No. 4000135355/21/I-DT-lr

Deliverable D2.3:

Validation Report (VR) on the cloud classification algorithm

Date: 07/06/2024

Version: 1.2

Authors:

T. Wagner, L. Reischmann, S. Beirle, S. Ziegler (MPIC)

A. Piters (KNMI)

F. Hendrick, M. Friedrich, M. Van Roozendael (IASB-BIRA)

A. Richter and Tim Bösch (IUP-UB)

U. Friess (IUP-HD)

M. Navarro and M. Yela (INTA)

A. Bais and D. Karagkiozidis (AUTH)

Content

Acronyms and abbreviations 4

References........ 4

1 Introduction 5

2 Validation approach........ 7

2.1 Selected stations and days 11

3 Validation results 12

3.1 Improvement of the definition of the temporal smoothness indicator (TSI) 14

3.2 Test of the thresholds used in the cloud classification algorithm 16

3.3 Additional test of the threshold value for the spread of the CI 18

4 Possible extension of the TSI to non-zenith viewing directions 23

5 Conclusions 25

Acronyms and abbreviations

Acronyms and abbreviated terms that are specific for this document can be found below.

DOAS	Differential Optical Absorption Spectroscopy
FRM_4DOAS	Fiducial Reference Measurements for Ground-Based DOAS Air-Quality Observations
RMS	Root mean square
SCD	Slant Column Density
dSCD	Differential Slant Column Density
SZA	Solar zenith angle
VCD	Vertical Column Density
WP	Work Package

References

[RD-1] FRM_4DOAS-2.0 deliverable D-2.1 'Technical Note on existing cloud classification algorithms'

Gielen, C., Van Roozendael, M., Hendrick, F., Pinardi, G., Vlemmix, T., De Bock, V., De Backer, H., Fayt, C., Hermans, C., Gillotay, D., and Wang, P.: A simple and versatile cloud-screening method for MAX-DOAS retrievals, Atmos. Meas. Tech., 7, 3509–3527, https://doi.org/10.5194/amt-7-3509-2014, 2014.

Takashima, H., Irie, H., Kanaya, Y., Shimizu, A., Aoki, K., and Akimoto, H.: Atmospheric aerosol variations at Okinawa Island in Japan observed by MAX-DOAS using a new cloud-screening method, Journal of Geophysical Research: Atmospheres, 114, https://doi.org/10.1029/2009JD011939, 2009.

Wang, Y., Lampel, J., Xie, P., Beirle, S., Li, A., Wu, D., and Wagner, T.: Ground-based MAX-DOAS observations of tropospheric aerosols, NO2, SO2 and HCHO in Wuxi, China, from 2011 to 2014, Atmos. Chem. Phys., 17, 2189–2215, https://doi.org/10.5194/acp-17-2189-2017, 2017.

Wagner, T., Apituley, A., Beirle, S., Dörner, S., Friess, U., Remmers, J., and Shaiganfar, R.: Cloud detection and classification based on MAX-DOAS observations, Atmos. Meas. Tech., 7, 1289–1320, https://doi.org/10.5194/amt-7-1289-2014, 2014.

Wagner, T., Beirle, S., Remmers, J., Shaiganfar, R., and Wang, Y.: Absolute calibration of the colour index and O_4 absorption derived from Multi AXis (MAX-DOAS measurements and their application to a standardised cloud classification algorithm, Atmos. Meas. Tech., 9, 4803–4823, https://doi.org/10.5194/amt-9-4803-2016, 2016.

1 Introduction

As clouds massively affect the atmospheric light paths, MAX-DOAS measurements under cloudy conditions can generally not be used for profile retrievals (see table 1). Thus, reliable cloud information is required in order to flag cloudy MAX-DOAS measurements as dubious or invalid. Beyond simple flagging, a cloud classification algorithm allows to investigate the effects of different cloud conditions for MAX-DOAS profile measurements separately. The determination of cloud properties from MAX-DOAS measurements themselves (instead of using independent cloud information) has several advantages. First, the cloud information can directly be assigned to the MAX-DOAS trace gas measurements without spatio-temporal interpolation. Second, the cloud algorithm can be used for MAX-DOAS measurements at different locations and with different availability of independent cloud information in a consistent way. Third, for situations with broken clouds, it might be possible to identify cloud contamination of individual elevation angles. Such cloud contaminated measurements might then be excluded from the profile inversion.

Table 1: Filter scheme of aerosol and trace gas results derived from MAX-DOAS observations. Filled circles: use of measurement is recommended; Open circles: use of measurement is not recommended. The table is taken from Wang et al., 2017.

	AOD	Aerosol extinction near surface	Profile of aerosol extinction	VCD	VMR near surface	Profile of VMRs
Low aerosol	•	•	•	•	•	•
High aerosol	•	•	•	•	•	•
Cloud holes	○	•	○	•	•	•
Broken clouds	○	•	○	•	•	•
Continuous clouds	○	•	○	•	•	•
Fog	○	○	○	○	○	○
Thick clouds	○	○	○	○	○	○

Clouds generally have a strong impact on the radiative transfer in the atmosphere. Thus, several quantities measured by the MAX-DOAS instruments are affected by clouds, can in turn be used for deriving cloud information. The main effects are:

A) Clouds are bright: Clouds typically increase the radiance compared to non-cloudy situations. However, e.g. in case of thick thunderstorm clouds, they might as well decrease the radiance. Thus, the radiance alone cannot be used in order to non-ambiguously identify clouds.

B) Clouds are white: The clear (blue) sky has a strong wavelength dependency for scattering probability (Rayleigh scattering), while scattering on cloud particles reveals almost no wavelength dependency. Thus, clouds look white. This effect on the broadband wavelength dependency of the radiance can be quantified by a color index (CI), i.e. the ratio of radiances for two different wavelengths. It has, however, to be noted that only in zenith view, clouds lead in general to a whitening of the sky. In non-zenith viewing directions, depending on the viewing geometry, the cloudy and clear sky can in principle have the same color.

C) As clouds alter atmospheric light paths, they directly affect the measured spectral signatures of "light path proxies" like the O_4 SCD; also the strength of the "Ring effect" is affected by clouds. However, as for the radiance, clouds might increase or decrease these quantities, depending on viewing geometry, sun position, and cloud height.

Since cloud conditions within the field of view of a MAX-DOAS telescope usually vary on short time scales (except for stratiform cloud cover), rapid changes of any of the quantities listed above indicate the appearance or disappearance of clouds or the change of cloud properties.

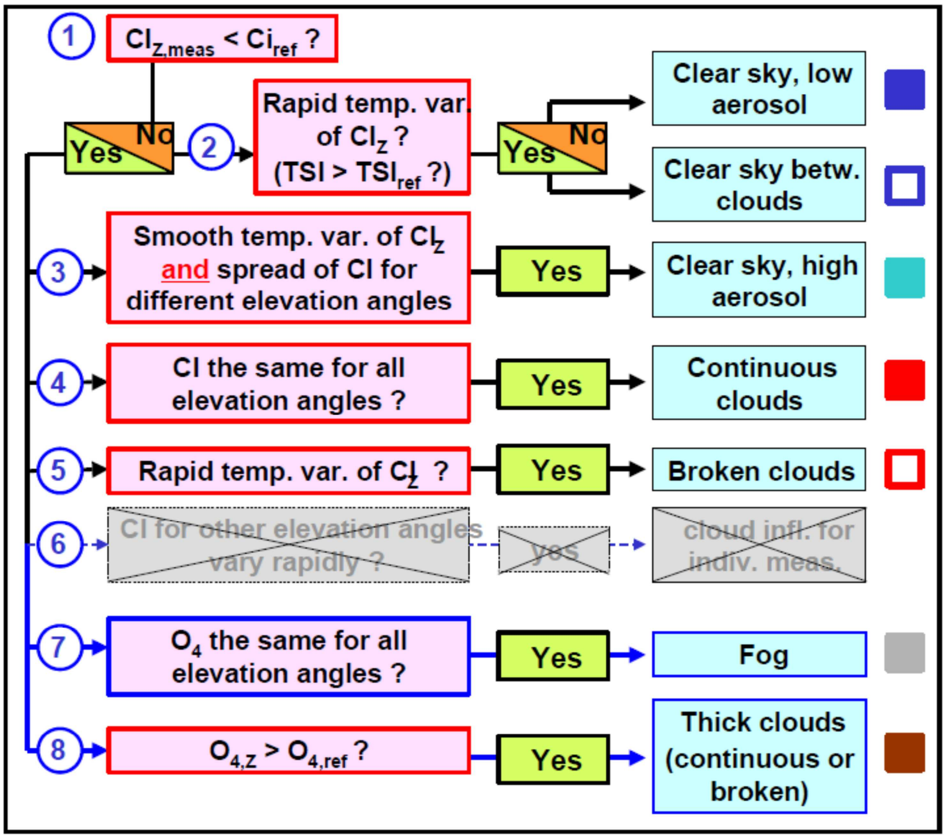

Figure 2: Cloud classification scheme. Paths with black arrows indicate the primary classification results: only one primary classification result can be attributed to a given elevation sequence. Paths with blue arrows indicate secondary classification results, which complement the primary classification results. The figure is taken from Wagner et al. (2014).

Cloud classification algorithms have been presented in different studies (Takashima et al., 2009; Gielen et al., 2014; Wagner et al., 2014, 2016; see also RD-1). They are based on the above mentioned quantities derived from MAX-DOAS observations. In this project, the multi-step algorithm by Wagner et al. (2014, 2016) was selected (see RD-1). This algorithm identifies clear sky conditions based on the absolute value of the CI in zenith direction, and uses its temporal variability to detect rapid changes in cloudiness, corresponding to clear sky between clouds or broken clouds. The variability of the CI with elevation angles is used to detect continuous clouds (low variability) or clear sky conditions with high aerosol load (high variability, while CI at zenith varies smoothly with time). In addition, in case of a low CI, the O_4 SCD and its elevation angle dependency are used to detect thick clouds and fog, respectively. The full scheme is shown in Fig. 2. So far the cloud algorithm was only applied in a limited number of studies. Moreover, no comprehensive and independent validation was performed. Such a validation was carried out within this project and is described in the following sections.

2 Validation approach

For the validation of the cloud algorithm, sky images were recorded and analysed visually. The sky images were recorded in two ways: first using a fish-eye camera to derive information about the overall sky conditions; second using a ‚telescope camera' (fixed to the moving telescope of the MAX-DOAS instrument) to characterise the sky conditions in the MAX-DOAS viewing direction. More information on the cameras and their operation is provided in Figs. 3 and 4.
Sky images as validation tool were chosen, because they allow a simple and direct categorisation of the sky condition by visual classification. Visual classification was chosen for simplicity and because automated techniques might fail in situations with complicated sky conditions. Nevertheless, in the future also more sophisticated automatic analysis techniques (in particular machine learning) might be used to classify the sky images. Another advantage of the use of sky images is that they allow the identification of the sky conditions also outside the direct field of view of the instrument, which will not be possible using other techniques with a narrow field of view like e.g. Lidars or ceilometers.

a) Telescope camera

Basetech Classic BS-WC-01 Webcam

640 x 480 Pixels
FOV: 45° x 65°
~6 EUR

b) Fish-eye camera

ELP 1080P Fisheye USB Full HD Camera

FOV: ~180°
2 megapixels
~50 EUR

Fig. 3 Specifications of the cameras and their preparation for the validation campaign. a) telescope camera; b) fish-eye camera.

Fig. 4 Left: Mounting of the telescope camera at the Tube MAX-DOAS instrument on the roof of the MPI for Chemistry in Mainz on 20.09.2022, 09:43 UTC. On this day it was occasionally raining. Center and right: camera images from the telescope camera and fish-eye camera, respectively, taken at the same time. Although some blurring is caused by the water drops on the foil, the sky conditions can be characterised.

Before the visual classification was performed, the exact location of the pointing direction of each MAX-DOAS telescope was determined. For that purpose, different methods were used. For the fish-eye cameras, the trace of the sun disk in the recorded images was analysed to determine the exact zenith direction (see Fig. 5). For the determination of the telescope direction within the telescope camera images, the position of the sun or an artificial light source was used (Figs. 6 and 7). For the Bremen instrument a combination of a lamp measurement and an elevation scan across the horizon was used.

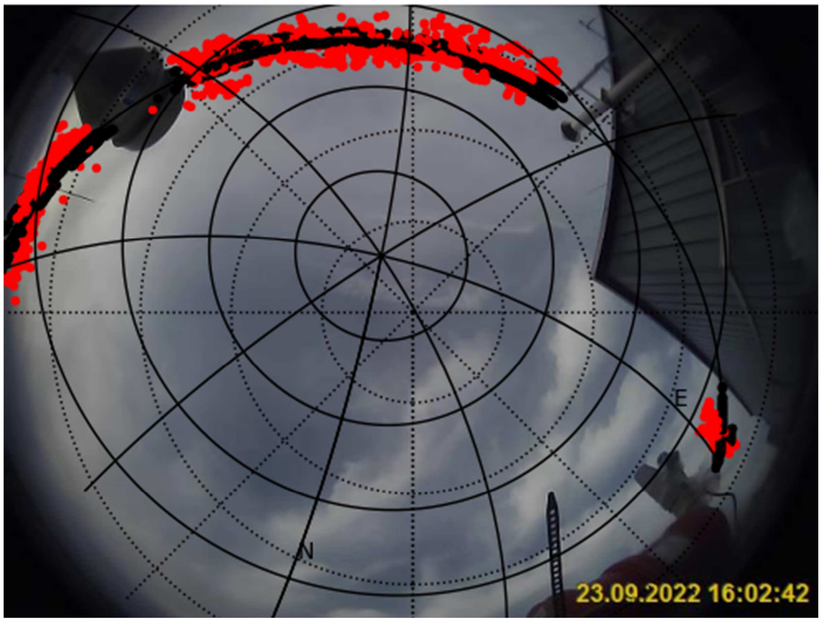

Fig. 5 Example of the determination of the exact location of the zenith direction within the fish-eye camera image for the Mainz instrument. The correct coordinate system was determined by fitting the calculated trace of the sun position (thick black line) to the observed sun positions (red dots). 5 camera-parameters (3 angles, translation, and scale) were fitted to match the observations. The dotted contours show the original coordinates, the solid contours the fitted coordinates. The center indicates the exact zenith direction. The calibration was performed by Ankie Pieters, KNMI.

Fig. 6 Left: Measurement set up for the determination of the location of the viewing direction within the image of the telescope camera. A light source in front of a black screen is placed in the field of view of the instrument. Right: image of the telescope camera after the telescope was turned into the direction for which the highest light intensity is received. The location of the light source in that image indicates the viewing direction of the telescope.

lamp position within the telescope camera image

sun position within the telescope camera image

measured intensity of the MAX-DOAS instrument as function of the telescope azimuth and elevation angle

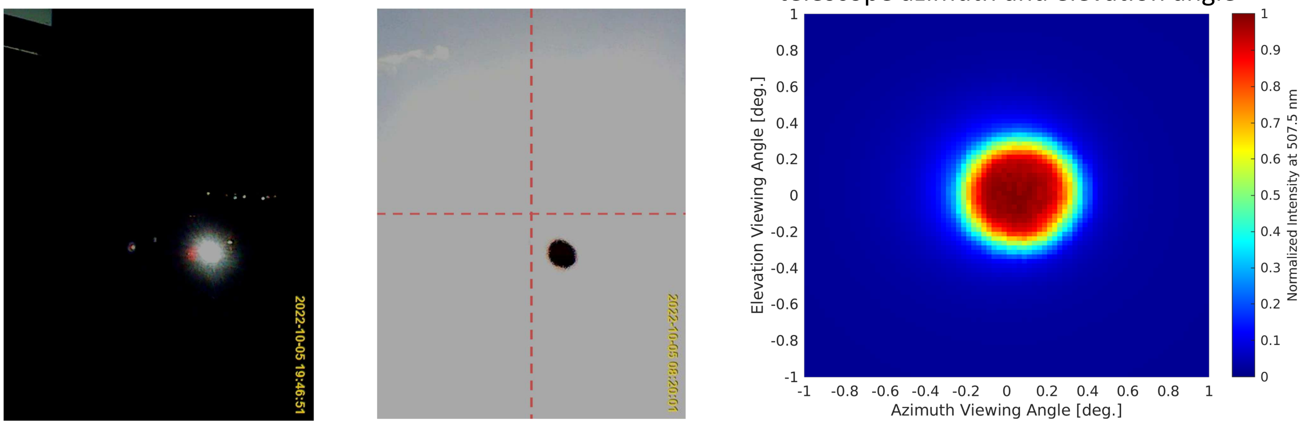

Fig. 7 Determination of the location of the telescope viewing direction within the image of the telescope camera for the instrument at Thessaloniki. The left and center images show the position of the lamp and sun within the image of the telescope camera. Right: the direction of the lamp was determined from the maximum intensity as function of the telescope azimuth and elevation angle.

For the visual classification of the sky condition a software tool created by MPIC was used. In that tool, the time series of the sky images can be continuously read and the visual classification result can be directly stored (see Fig. 8). In that way a large number of images can be classified in an efficient way.

The visual classification was performed in two ways: either only the zenith direction was considered (within approximately the 10° circle around zenith), or the complete set of images for all elevation angles was considered. The latter classification results could potentially be used for the possible validation of the cloud classification of individual elevation angles. However, since this information is not available for the current version of the cloud classification algorithm, only the first set of visual classifications based on the zenith observations was used. They fit better to the results of the cloud classification algorithm, which as well are mainly based on the zenith observations. Nevertheless, the second set of visual classifications including also the non-zenith measurements might be used in future validation exercises, when cloud classification results are also available for non-zenith viewing directions.

In order to increase the robustness of the results, the visual classification was performed in two successive rounds.

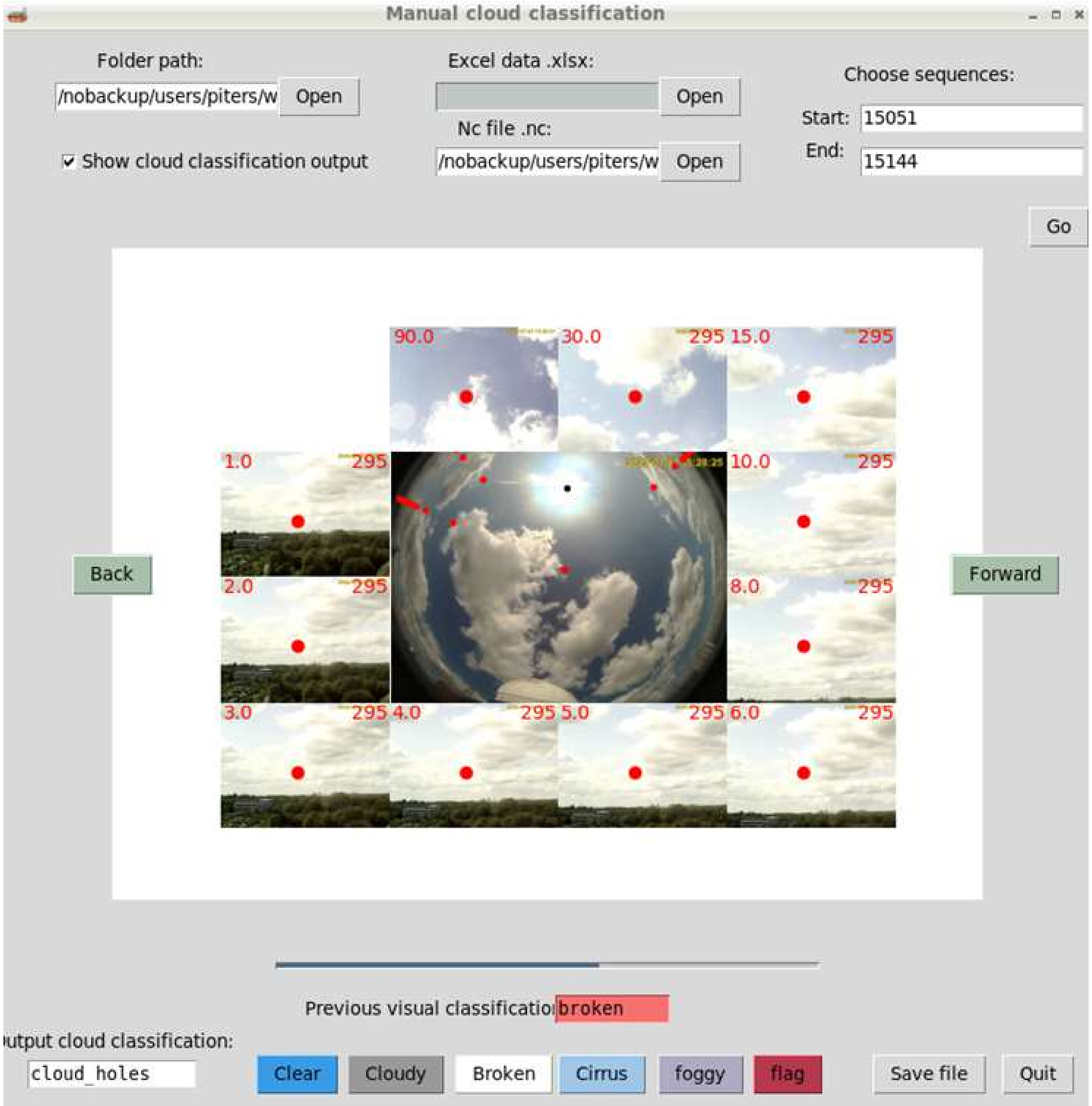

Fig. 8 Software tool used for the visual classification of the sky conditions. The center shows an image of the fish-eye camera taken within 5 min of the MAX-DOAS zenith observation. The surrounding images show pictures of the telescope camera for the different elevation angles (taken within 1 min of the MAX-DOAS measurements). The buttons at the bottom are the different choices for the visual cloud classification. The software tool was developed by Lucas Reischmann, MPIC.

2.1 Selected stations and days

Five project partners agreed to operate both cameras together with their MAX-DOAS instrument for a period of several months. The locations of the MAX-DOAS instruments are at latitudes between about 40° N (Thessaloniki) and 53°N (Bremen), see table 2.

In order to limit the validation effort, the visual classification of the sky conditions was restricted to only four days per measurement location (see table 2). From these four days, one day was mostly clear, a second mostly cloudy, and on the remaining two days mostly broken clouds were present. In table 2 an overview on the selected days at each station is provided.

Table 2 Selected days used for the validation study at the different locations

Location	**Mostly clear day**	**Mostly cloudy day**	**Days with mostly broken clouds**
Bremen	19.07.2022	22.07.2022	23.07.2022, 28.08.2022
Cabauw	11.08.2022	09.06.2022	16.08.2022 17.08.2022
Uccle	19.07.2022	21.07.2022	03.07.2022 15.07.2022
Mainz	22.09.2022	29.09.2022	19.09.2022 23.09.2022
Thessaloniki	07.07.2022	18.06.2022	20.06.2022 26.06.2022

3 Validation results

The results of the cloud classification algorithms and of the visual classification cannot be directly compared, because the respective sky categories are not exactly the same. Fig. 9 shows the relationships between both classifications. The visual classification results for clear skies and broken clouds are each assigned to two categories of the classification algorithm. For continuous clouds and fog, direct assignments are possible. For the category ‚cirrus' from the visual classification, no perfect category from the classification algorithm is available. In the following we assigned 'cirrus' to the categories clear sky conditions with low aerosol load and clear sky conditions with high aerosol load.
In Fig. 10 the validation results are shown. The columns represent the visual classifications, the lines the results of the classification algorithm. The boxes surrounded by the solid lines represent successful assignments; the boxes outside the solid lines represent wrong assignments. In total 1443 elevation sequences were compared. The numbers at the right side and the bottom show the results of the confusion matrix for the merged cases (clear & cirrus, broken, clouds, and fog, see Fig. 9), see e.g. https://en.wikipedia.org/wiki/Confusion_matrix. The red values at the right side represent the errors of commission: the fraction of values that were predicted by the classification algorithm to be in a class but do not belong to that class according to the visual classification (false positives). The red values at the bottom represent the errors of omission: the fraction of values that values that belong to a class according to the visual classification, but were predicted classification algorithm to be in a different class (false negatives).
The overall accuracy of the cloud classification algorithm was found to be 56.6%.

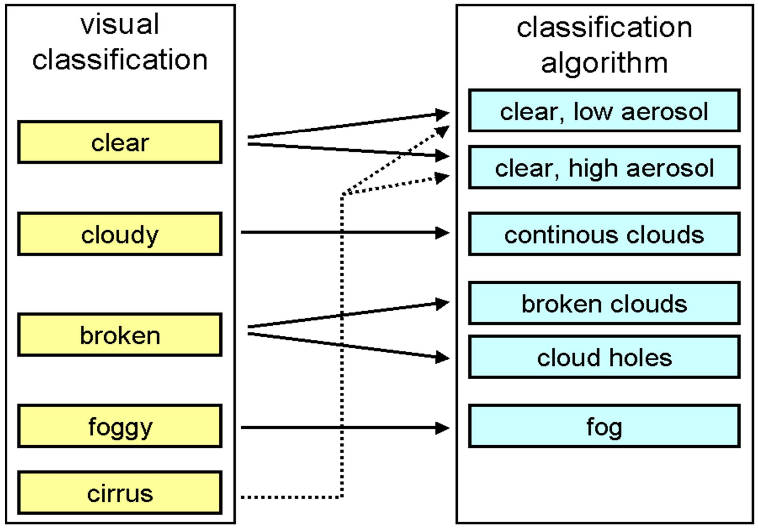

Fig. 9 Relationships between the categories of the visual classification and the cloud classification algorithm used for the comparison of both data sets.

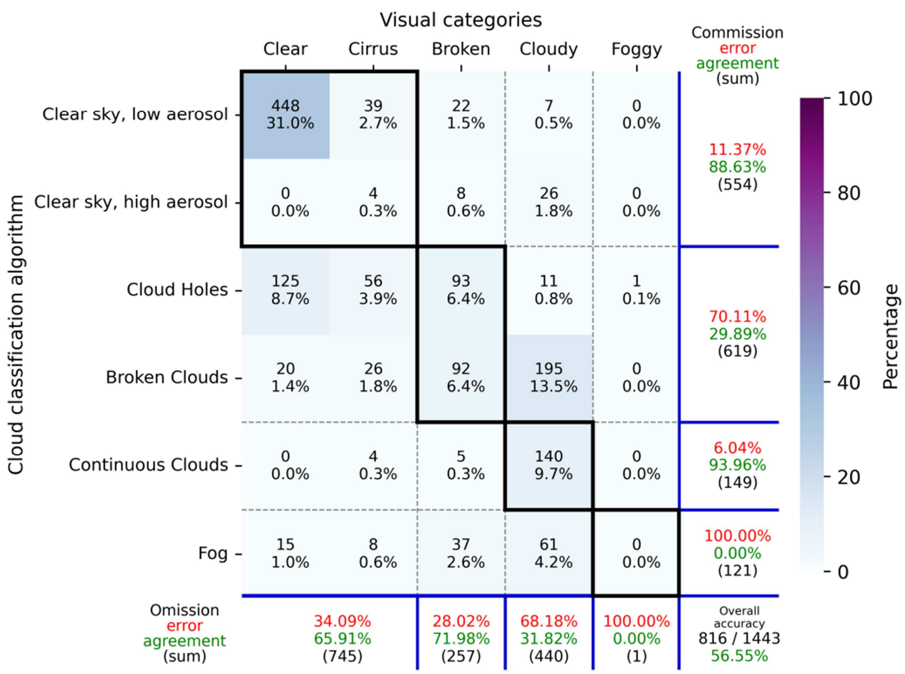

Fig. 10 Validation results using the visual classification. The columns indicate the visual classifications, the lines the results of the classification algorithm. The boxes surrounded by the solid lines represent successful assignments; the boxes outside wrong assignments. The numbers in the boxes show the number of cases (top) and the corresponding percentages (bottom). At the right side and the bottom, the results of the confusion matrix for the merged cases (clear & cirrus, broken, clouds, and fog, see Fig. 9) are shown. The red values at the right side represent the errors of commission (false positives), the red values at the bottom represent the errors of omission (false negatives, for details see text). In total 1443 elevation sequences were considered. The overall accuracy is 56.6%.

Three main problems of the cloud classification algorithm were identified:

A) Only about 74% of all clear sky situations were correctly identified by the cloud classification algorithm (448 out of in total 608 cases). Many clear sky cases were wrongly assigned to the category ‚cloud holes'. This finding indicates that the threshold for the temporal smoothness indicator (TSI) used in Wagner et al. (2016) is too strict.

B) About 50% of all overcast (cloudy) situations were wrongly assigned as broken clouds (195 out of in total 389 cases). Only 35% were assigned to the category ‚continuous clouds' (141 out of in total 389 cases). Again, this finding indicates that the threshold for the temporal smoothness indicator (TSI) is too strict.

C) 87.5% of the sequences classified as clear sky cases with high aerosol load are assigned to cloudy situations. This problem indicates that the threshold for the spread of the color index is too high. Here, however, it should be noted that the validation results are only based on a small percentages of all cases.

Also a few measurements categorised as 'fog' are misclassified as 'clear'. The reason for this misclassification is currently not understood. Because of the low number of cases the existing data set is not well suited to further investigate this discrepancy. Thus additional measurements with more fog situations are needed in future studies to better understand and possibly improve this shortcoming.

In the next sections, the aspects listed above are further investigated and corresponding improvements are developed.

3.1 Improvement of the definition of the temporal smoothness indicator (TSI)

Equation 1 shows the definition of the TSI as in Wagner et al. (2016):

$$TSI_{n,orig} = \left[\frac{CI_{n+1} - CI_{n-1}}{2} - CI_n \right] \quad (1)$$

CI_n indicates the colour index of the zenith measurement at the beginning of the n^{th} elevation sequence. In cases of a monotonous increase of the CI for three successive zenith observations, this definition of the TSI yields values close to zero, because the changes of the CI between the preceding and succeeding zenith observations largely cancel each other. To avoid this problem, the absolute changes of the CI of the preceding and succeeding zenith observations are calculated instead:

$$TSI_{n,corrected} = \left[\frac{|CI_n - CI_{n-1}| - |CI_n - CI_{n+1}|}{2} \right] \quad (2)$$

Now, however, a new complication arises even on clear days, the CI changes systematically with the solar zenith angle (SZA). With the corrected TSI definition, such monotonous changes will yield TSI > 0 erroneously indicating changing sky conditions, e.g. ‚cloud holes'. To overcome this problem, the CI has to be normalised before the TSI is calculated. For the normalisation the dependence of the CI on

SZA for an optical depth of 0.2 (at 390 nm) was chosen (see Fig. 11). This AOD value was chosen, because it fits typical situations, but will of course not fit to extreme cases. The polynomial expression for the SZA dependence of the CI is:

$$CI_{AOD=0.2}(S) = 13.144 \cdot S^6 - 39.445 \cdot S^5 + 47.422 \cdot S^4 - 31.335 \cdot S^3 + 10.383 \cdot S^2 - 0.5107 \cdot S + 1.0026 \quad (3)$$

Here S indicates the SZA in degrees divided by 90.

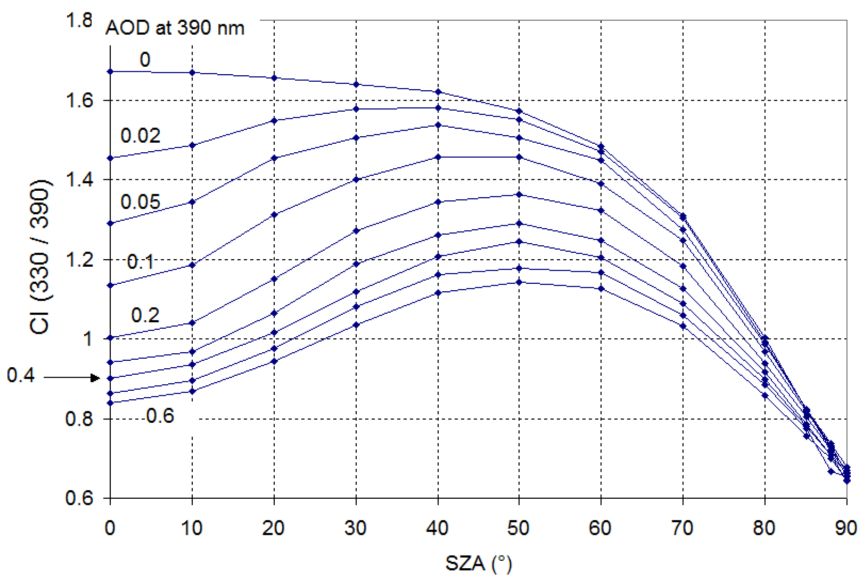

Fig. 11 Dependence of the CI on SZA for different aerosol optical depths (at 390 nm). For the normalisation of the measured CI, the results for an AOD of 0.2 were chosen.

To achieve consistency with the original definition, also the original threshold is normalised (divided) by the SZA dependence.

Another update was applied to the TSI definition. The calculation according to equation 2 was finally replaced by the following definition:

$$TSI_{n,new} = \left| CI_{n,start} - CI_{n,end} \right| \quad (4)$$

Here $CI_{n,start}$ and $CI_{n,end}$ indicate the CI of the zenith observation before and after the selected elevation sequence. This new definition was introduced to avoid the asymmetry of the original definition.

3.2 Test of the thresholds used in the cloud classification algorithm

As indicated by the validation results, the threshold values for the TSI and the spread of the CI need to be tested and probably adjusted. For that purpose, the visual classification results for the selected days were used again and the dependence of the fractions of correct assignments on the variation of the thresholds (including also the threshold for the CI) is investigated. The corresponding results are shown in Figs. 12 to 14.

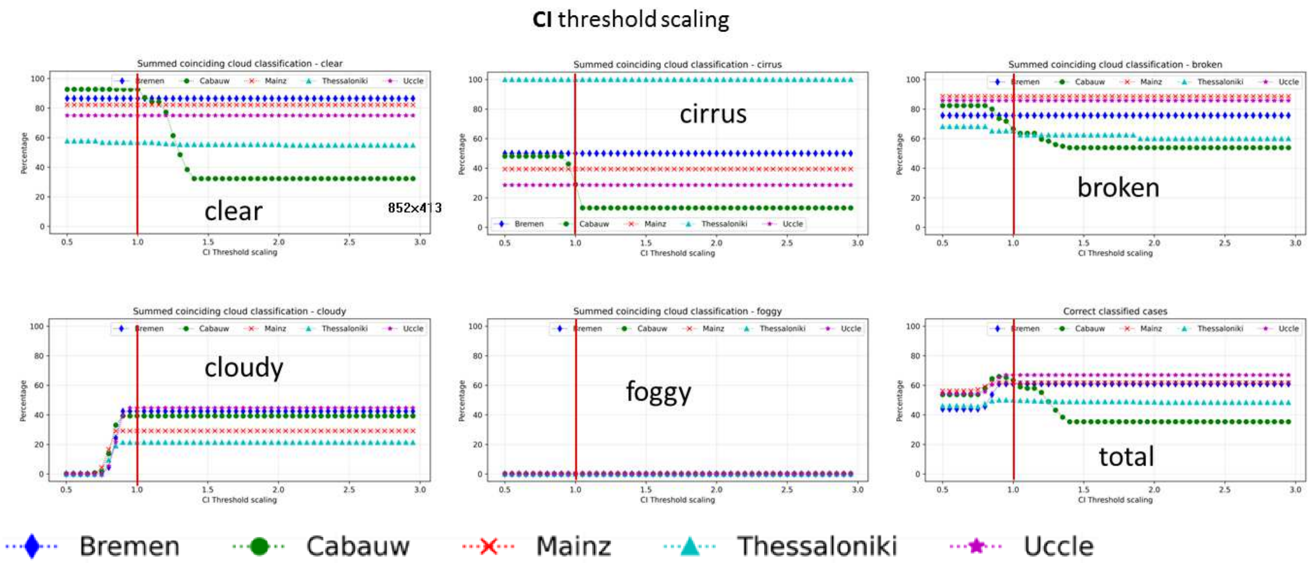

Fig. 12 Dependence of the fraction of correct assignments of the classification algorithm on the threshold for the CI. The figure at the bottom right presents the results for all categories.

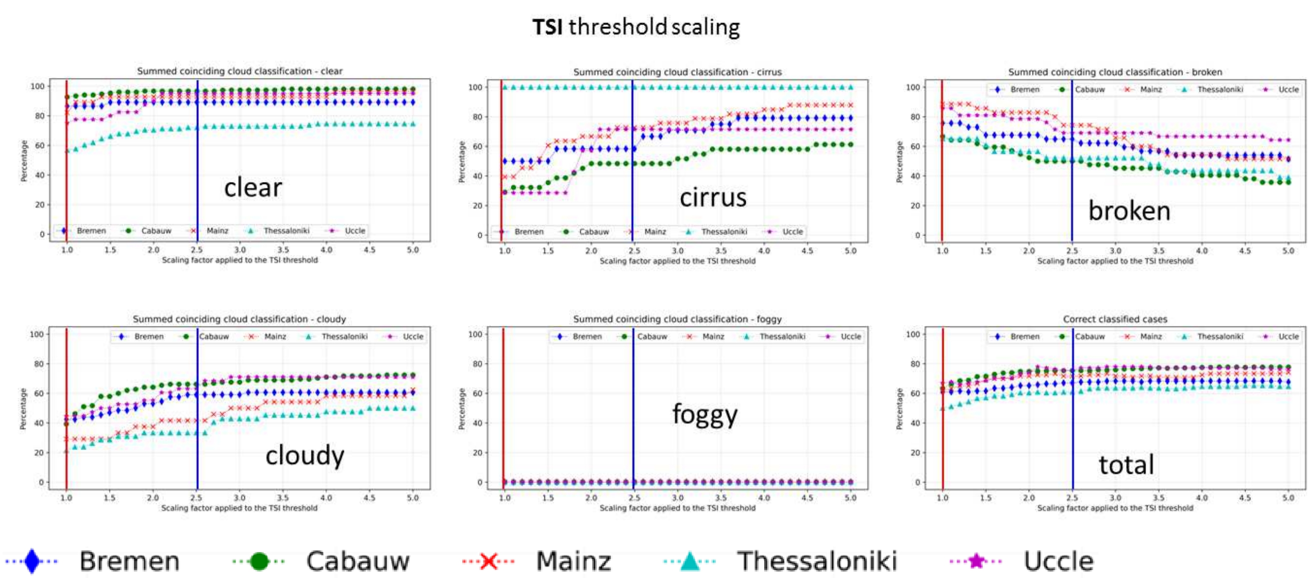

Fig. 13 Dependence of the fraction of correct assignments of the classification algorithm on the threshold for the temporal smoothness indicator. The figure at the bottom right presents the results for all categories.

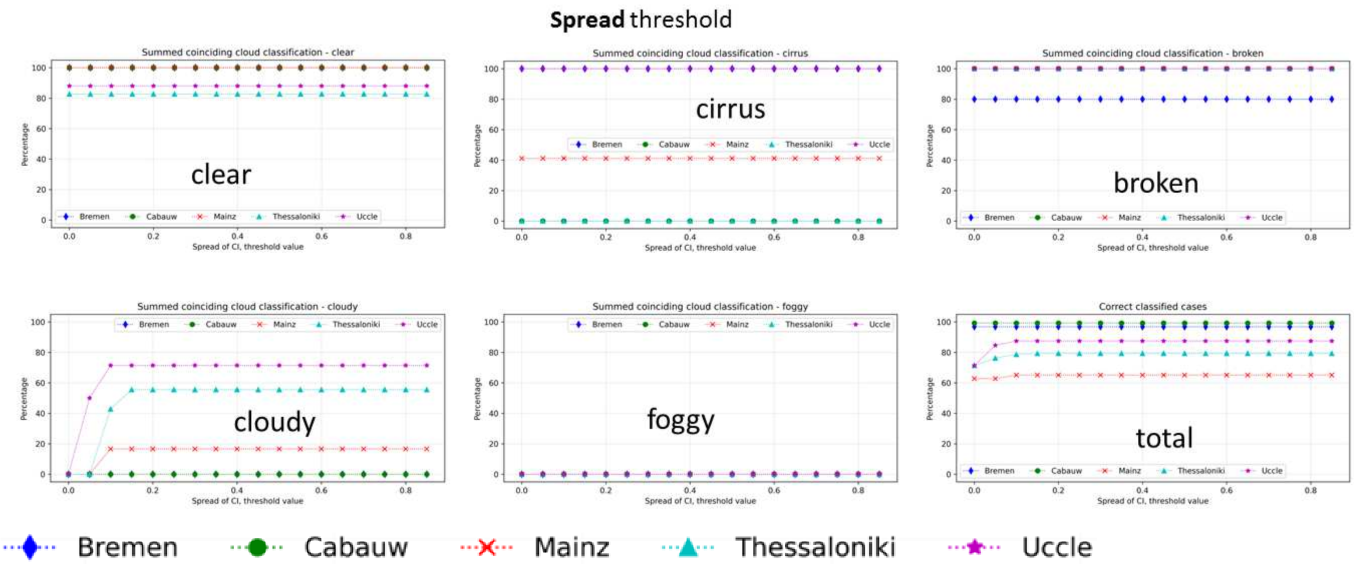

Fig. 14 Dependence of the fraction of correct assignments of the classification algorithm on the threshold for the spread of the CI. The figure at the bottom right presents the results for all categories.

For the threshold of the CI, the results show a maximum of correct assignments for values around the original threshold. Therefore, the original threshold was kept.
For the threshold of the temporal smoothness indicator, the fraction of correct assignments for clear or cloudy situations increase up to about a threshold of 2.5 times the original value (as in Wagner et al., 2016). This indicates that during clear and cloudy sky conditions, the variation of the CI is often much higher than represented by the original threshold. Therefore, in the updated algorithm, a new threshold of 2.5 times the original threshold will be used. Nevertheless, also the original threshold will be used as an additional criterion. Clear and cloudy cases with TSI below even the original threshold represent situations with peculiar stable atmospheric conditions (see Fig. 15). It will be interesting to see how the MAX-DOAS profile inversion results differ for cases which fulfill also the more strict (original) atmospheric stability criterion.

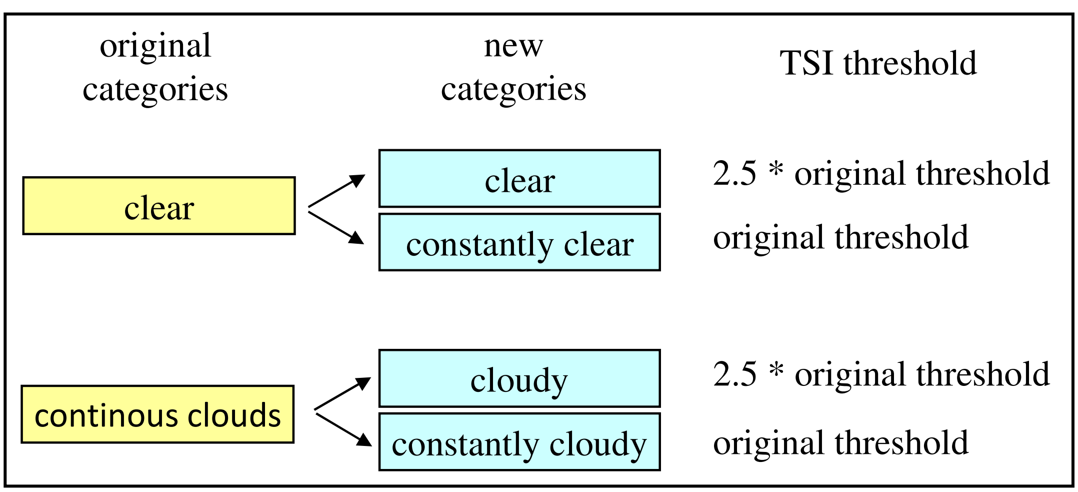

Fig. 15 Introduction of new categories based on different threshold values for the temporal smoothness indicator. The categories 'constantly clear' and 'constantly cloudy' are sub categories of 'clear' and 'cloudy'.

For the threshold of the spread of the CI, no clear conclusions can be drawn because of the low number of cases of clear sky conditions with high aerosol load (see Fig. 10). Also for the days selected for the validation, almost no situations with high AOD occurred. Therefore the threshold value for the spread of the CI was investigated using a different set of measurements in the next section.

3.3 Additional test of the threshold value for the spread of the CI

The threshold for the spread of the CI was tested using the MAX-DOAS measurements at Seoul. These measurements were carried out with the same instrument in the 8 months directly before the measurements in Mainz. The instrumental properties were almost identical to those during the Mainz measurements. Thus the cloud classification algorithm could be applied consistently to both the measurements in Mainz and Seoul.
Measurements in Seoul are well suited for the test of the threshold for the spread of the CI, because in Seoul often high AOD occur. Moreover, from simultaneous AERONET measurements, exact AOD data are also available. For the following investigation, only measurements with a maximum time difference of 10 min between MAX-DOAS and AERONET measurements were considered.

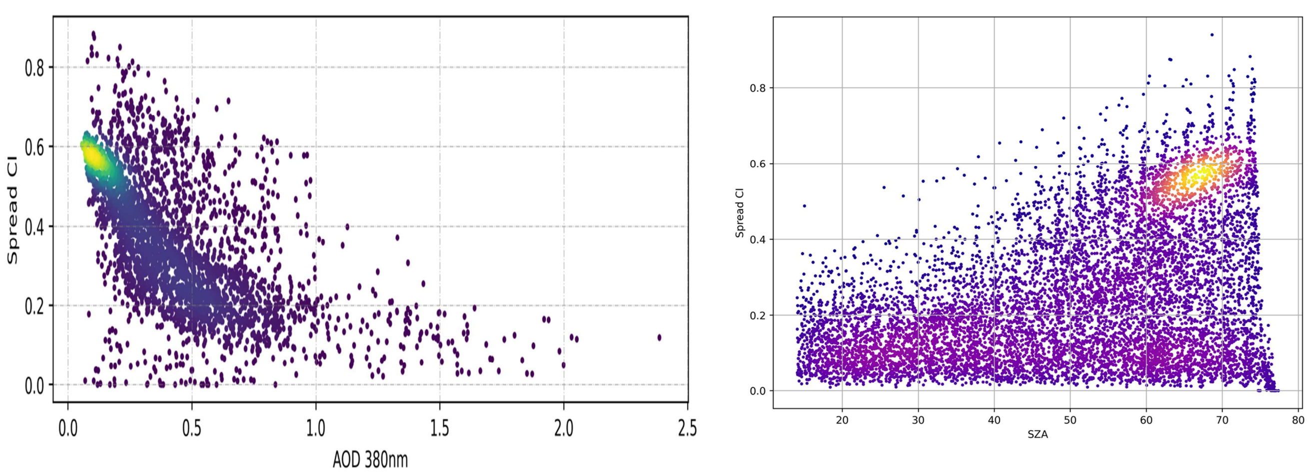

Fig. 16 Dependence of the spread of the CI as function of the simultaneously measured AOD from an AERONET sun photometer (left) and SZA (right) for measurements in Seoul.

In Fig. 16 the dependencies of the spread of the CI as function of the AOD and SZA are shown. Clear dependencies on both quantities are found. The SZA dependence is also found in radiative transfer simulations, especially for clear sky situations with different aerosol loads (Fig. 17 left). For cloudy situations, only a weak dependence of the spread of the CI on the SZA is found (Fig. 17 right). Interestingly, the difference of the spread of the CI between clear and cloudy situations vanishes for small SZA (< about 40°). Thus the spread of the CI cannot be used for such small SZA to distinguish between situations with clear sky with high aerosol loads and cloudy sky.

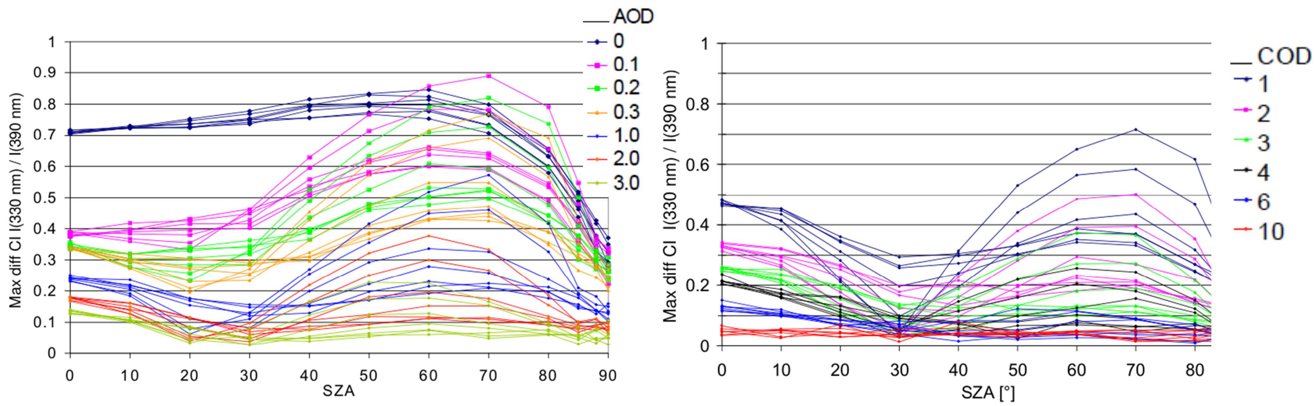

Fig. 17 Spread of the CI for different aerosol (left) and cloud (right) scenarios derived from radiative transfer simulations. The different lines of the same colour represent simulations for different relative azimuth angles (0, 30, 60, 90, 120, 150, 180). (Fig. A2 in Wagner et al., 2016)

The SZA dependence shown in Fig. 17 is approximated by a polynomial fitted to the simulation results for AOD of 0.1 and 0.2:

$$\text{spread}_{\text{AOD } 0.1,\ 0.2} = -0.38 \cdot S^6 + 3.4836 \cdot S^5 - 9.186 \cdot S^4 + 6.2471 \cdot S^3 + 0.0513 \cdot S^2 - 0.318 \cdot S + 0.3716 \tag{5}$$

with S being the SZA in degrees divided by 90. The polynomial is shown in Fig. 18.

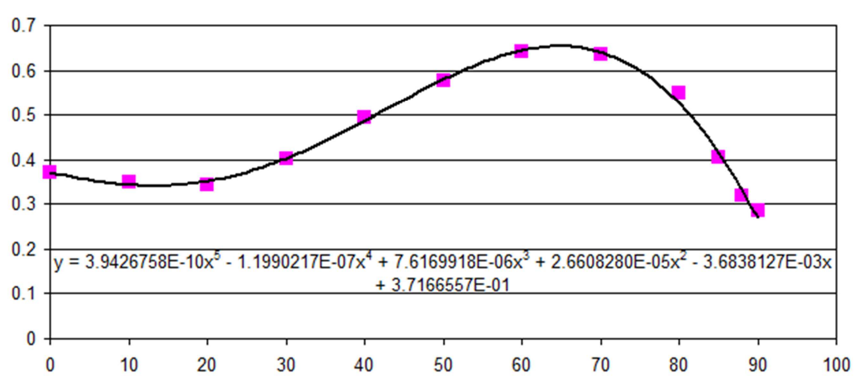

Fig. 18 Average dependence of the simulated spread of the CI on the SZA for AOD of 0.1 ad 0.2 (Fig. 17 left). The fitted polynomial is given in equation 5.

To account for the SZA dependence, the measured spread of the CI is normalised (divided) by the polynomial. Like for the original spread of the CI also after the normalisation a systematic dependence on the AOD is found (Fig. 19), from which a new threshold value for the normalised spread of the CI is derived. The new threshold value of 0.5 indicated by the horizontal red lines corresponds to an AOD of about 0.5 (red vertical lines).

Interestingly, different overall AODs for small and high SZA are found. This apparent dependence, however, can be explained by the seasonal variation of the AOD in Seoul (Fig. 20).

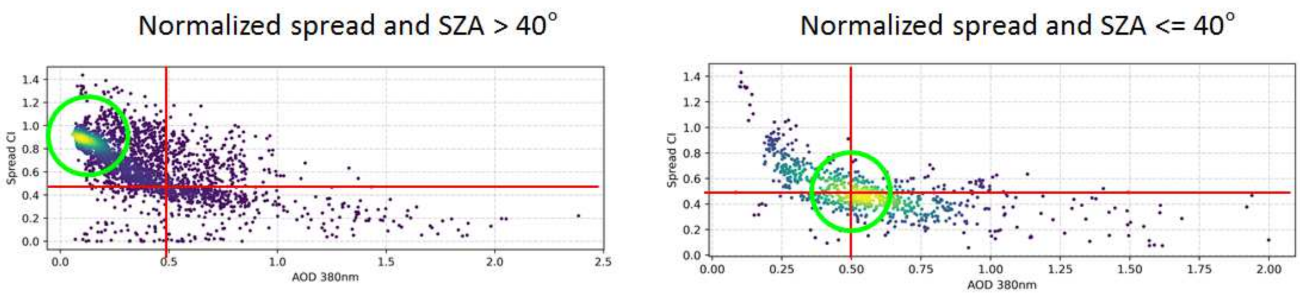

Fig. 19 Dependence of the normalised spread of the CI on the AOD for SZA > 40° (left) and <40° (right).

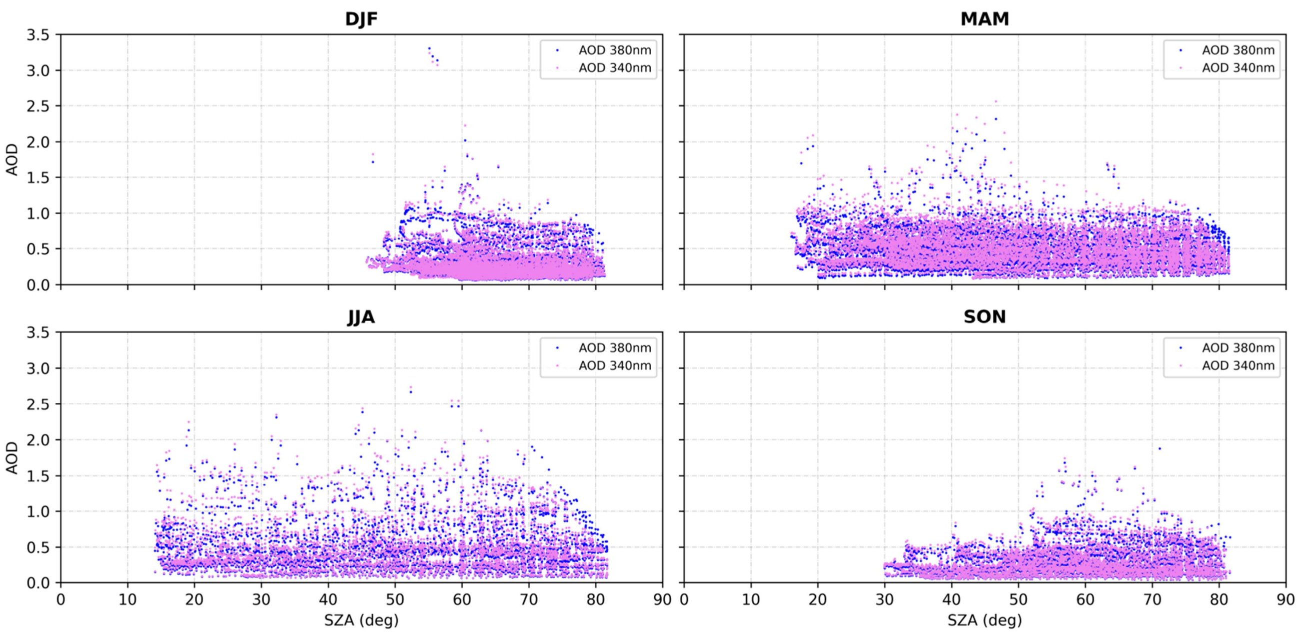

Fig. 20 AOD measured by the sun photometer at Seoul for different seasons. High values are mostly found in spring and summer.

The normalisation of the spread and the new threshold is included in the cloud classification algorithm. The results for the updated categories of clear sky conditions with low and high aerosol loads are shown in Fig. 21 as function of the AOD. Clear sky conditions with low aerosol load are mostly found for AOD < 0.7; clear sky conditions with high aerosol load are mostly found for AOD > 0.7. Thus the normalisation of the spread of the CI and the new threshold value of 0.5 are well suited to distinguish between situations with high and low AOD.

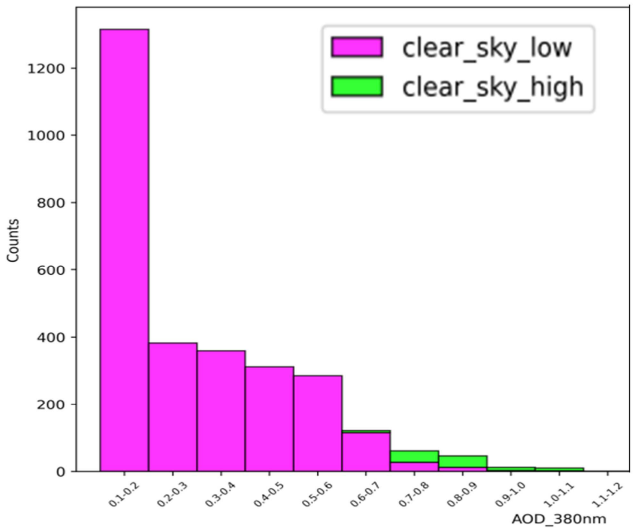

Fig. 21 Dependence of the occurrence of the classification categories of clear sky with high or low aerosol load on the AOD from AERONET.

Effect of the updates of the cloud classification algorithm on the validation results

In this section the effects of the different changes of the cloud classification algorithm on the validation results are presented. The different changes are applied step by step. Fig. 22a shows the initial validation results of the cloud classification algorithm as already presented in Fig. 10. If, however, only measurements with SZA < 75° are considered as recommended by Wagner et al. (2014, 2016), the overall accuracy improves (Fig. 22b). After application of the new TSI definition (section 3.1) the results are almost unchanged (Fig. 22c).

An important change occurs if the newly defined so called change flag is applied. The change flag marks sequences with different classification results for the preceding or succeeding sequences. The results in Fig. 22d represent only sequences for which the change flag indicates no such changes. The application of the change flag largely improves the overall accuracy (from about 61% to 89%). However, at the same time, the number of considered cases is reduced by more than a factor of 3. Fortunately, the application of the change flag mainly affects situations with broken clouds which are the most unfavorable conditions for MAX-DOAS profile inversions.

Fig. 22e presents validation results after the threshold for the TSI was enhanced by a factor of 2.5. This change further improves the overall accuracy to almost 94%. Also the number of considered cases increases slightly again.

a) no SZA limit

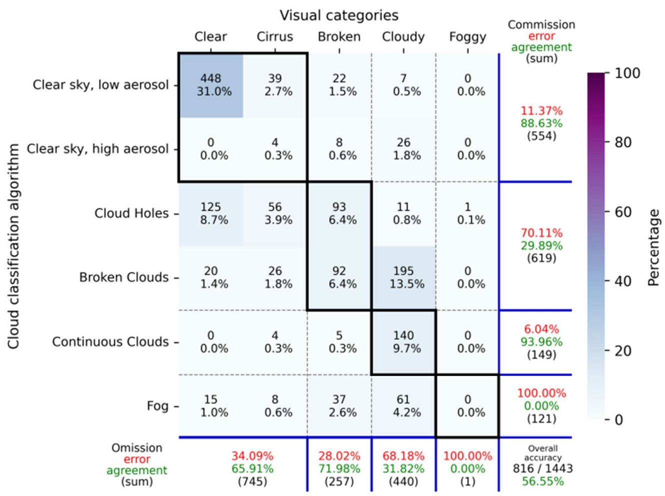

b) SZA < 75°

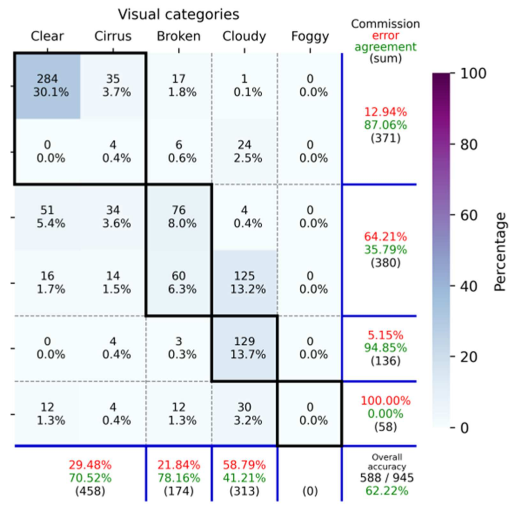

c) new TSI

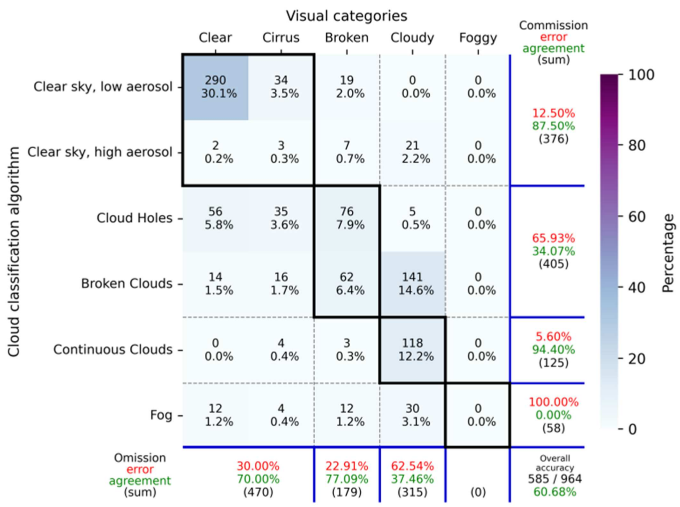

d) consideration of change flag

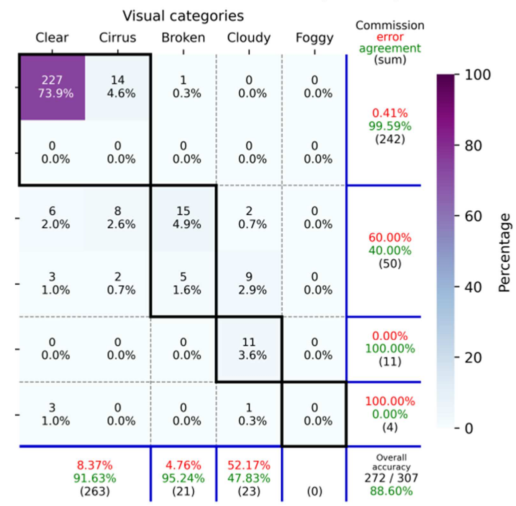

e) TSI threshold multiplied by 2.5

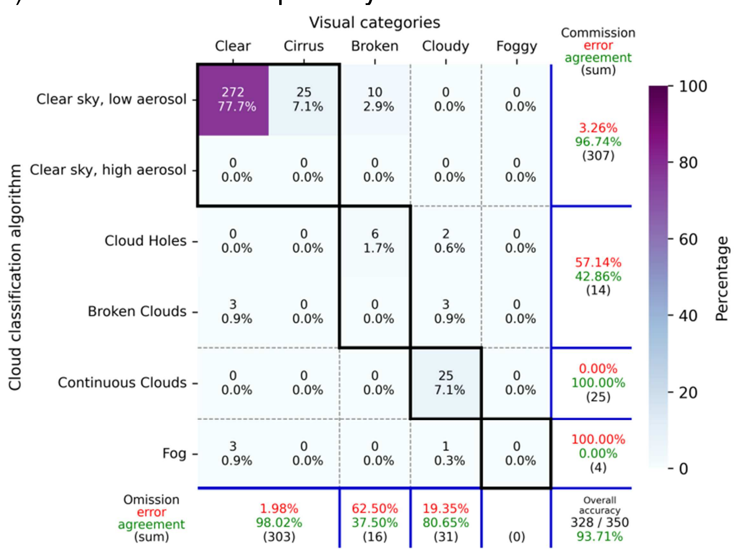

Fig. 22 Changes of the validation results after several modifications are applied step by step. a) initial validation results; b) results if only SZA <75° are considered; c) after the update of the TSI definition; d) if the ‚change flag' is considered; after the TSI threshold is multiplied by a factor of 2.5. For details, see Fig. 10.

4 Possible extension of the TSI to non-zenith viewing directions

One of the initial aims of this work package was the possible extension of the cloud classification to individual measurements within an elevation sequence. The most promising approach for such an extension is the application of the TSI also to non-zenith viewing directions. However, because the atmospheric light paths for non-zenith viewing directions are usually longer than for zenith direction, the probability of light scattering into the line of sight by molecules and aerosols is also larger than for zenith direction. Thus the relative change of the radiances and the CI caused by clouds is weaker than for observations in zenith direction and the TSI threshold used for zenith direction cannot be directly applied to measurements at lower elevation angles. To determine suitable TSI thresholds for the non-zenith directions, again the measurements made in Mainz and Seoul were considered. They cover a period of 10 months including many measurements with changing cloud conditions.

For these measurements, the TSI was calculated individually for all elevation angles, and the TSI for the non-zenith viewing directions are plotted versus the TSI for zenith direction of the same elevation sequence. The results are presented in Fig. 23. Rather weak correlations are found for the non-zenith elevation angles (except for 30°). The low correlations are mainly caused by the different target areas of the non-zenith directions compared to zenith view, because especially for situations with broken clouds, the exact cloud situation in different parts of the sky is usually quite different. In spite of the low correlations, there are weak dependencies of the slopes and the maximum TSI on the elevation angle. These dependencies indicate that the TSI is probably a useful quantity to identify cloud contamination also for low elevation angles. Nevertheless, more investigations are needed to exploit the full potential of this possibility. Two strategies could be used to further assess the potential of the TSI for non-zenith directions:

a) MAX-DOAS profile inversion results should be performed using either all elevation angles or only elevation angles, for which the TSI values are below the respective thresholds. Then the performance of both profile inversions should be compared, e.g. by the assessment of the consistency of the results or by comparison to independent measurements.

b) The smoothness of the retrieved trace gas dSCDs within an elevation angle should be considered. It should be investigated if outliers in these sequences correspond to measurements with enhanced TSI, the TSI for non-zenith elevation angles. If that was the case, the TSI is probably a useful quantity also to identify cloud contaminated individual measurements.

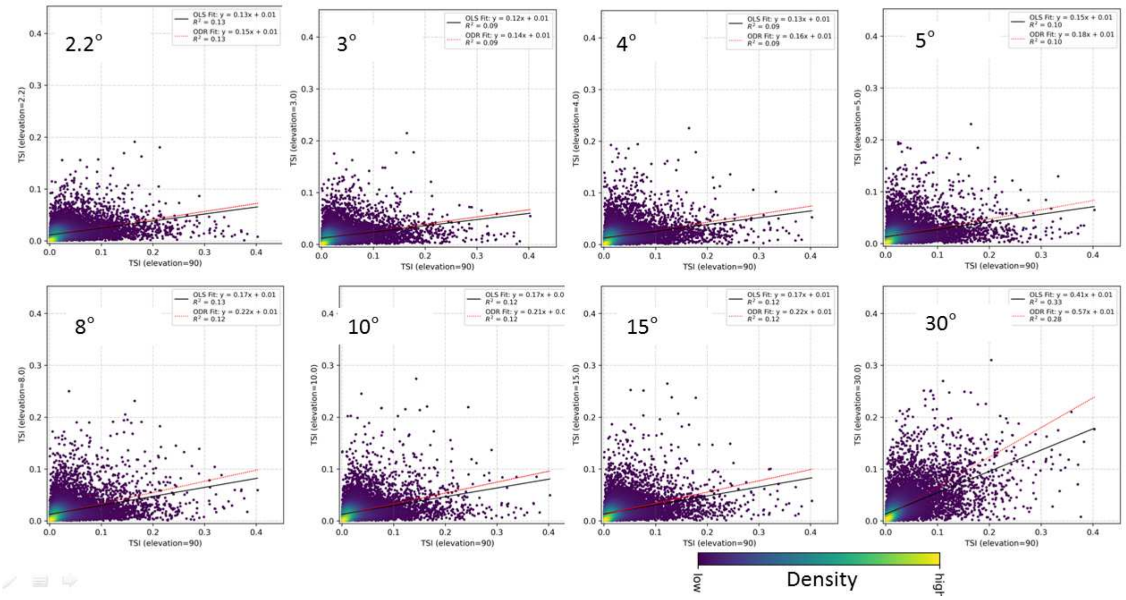

Fig. 23 Correlation plots of the TSI for non-zenith viewing directions versus the TSI for zenith direction of the same elevation sequence.

a) correlation coefficient

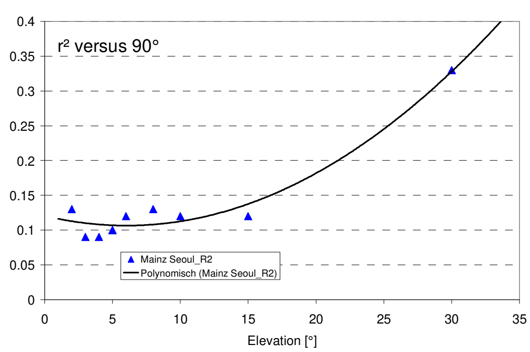

b) slope from linear fit

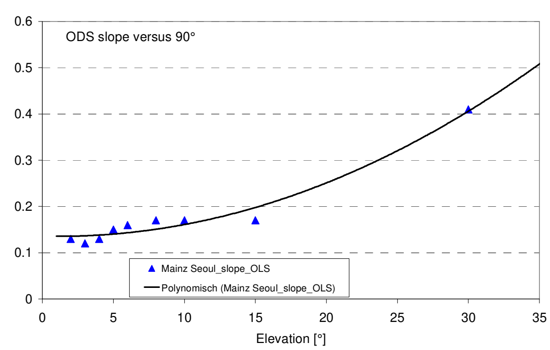

c) maximum TSI

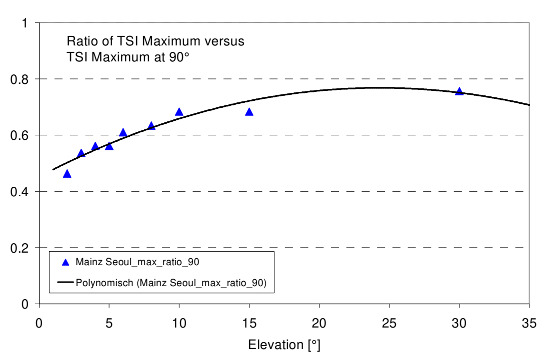

Fig. 24 a) elevation dependence of the correlation coefficients (r^2) of the TSI for non-zenith directions versus the TSI for zenith direction. b) elevation dependence of the slope of the TSI for non-zenith directions versus the TSI for zenith direction. c) elevation dependence of the maximum TSI.

5 Conclusions

In this work package the cloud classification algorithm introduced in Wagner et al. (2014; 2016) was applied to MAX-DOAS measurements at 5 locations in Europe. The obtained classification results were compared to simultaneous recorded sky images, which were analysed by visual inspection. For each station, 4 days were selected, one clear and one cloudy day, as well as two days with broken clouds. The initial validation results showed moderate agreement of the cloud classification results with the validation data set with an overall accuracy of slightly more than 50%. Based on these results, several improvements were applied to the cloud classification algorithm. After these improvements were applied, the overall accuracy increased to more than 90%.

Also an attempt was made to extend the application of the TSI to non-zenith viewing directions. It was found that the TSI is probably a useful quantity also for the identification of a cloud contamination of individual measurements. But here further research is needed. Suggestions were made for further investigations to explore the full potential of this approach.